ROYAL SOCIETY
OF CHEMISTRY

PAPER

Check for updates

Dual-phase Yb-doped La$_2$Ce$_2$O$_7$ materials for fuel flexible SOFCs†

Bishnu Choudhary [ID] *[ab] and Shahid Anwar [ID] *[ab]

La$_{2-x}$Yb$_x$Ce$_2$O$_7$ (where x = 0, 0.05, 0.10, 0.15, and 0.20) has been studied as a possible electrolyte material for solid oxide fuel cells (SOFCs), demonstrating a novel material. Nanosized La$_{2-x}$Yb$_x$Ce$_2$O$_7$ ceramics have been synthesized *via* the glycine nitrate combustion method. To elucidate the dual phase character (F-type and C-type phase) present in the Yb-doped La$_2$Ce$_2$O$_7$, extensive X-ray diffraction and Raman spectroscopy analyses have been performed to thoroughly investigate the crystal structure and phases. Furthermore, doping has been shown to affect the dual phases present in the system. The ionic conductivity and the space charge potential of the Yb-doped La$_2$Ce$_2$O$_7$ have been analyzed in details and the highest ionic conductivity of 3.3×10^{-3} S cm^{-1} at 700 °C is achieved at x = 0.05. Therefore, the La$_{1.95}$Yb$_{0.05}$Ce$_2$O$_7$ composition has been chosen for the electrophoretic deposition (EPD) for SOFCs fabrication. The La$_{1.95}$Yb$_{0.05}$Ce$_2$O$_7$ film, coated using EPD in isopropanol, is found to be crack-free and dense with a thickness of approximately 14 μm. The maximum power density of the fabricated cell is observed to be 589 and 420 mW cm^{-2} at 700 °C in wet hydrogen and methane fuel, respectively. Impedance spectrum analysis utilizing the distribution of relaxation time (DRT) analysis shows that the gas diffusion process in the electrodes plays a significant role in the overall polarization of the cell.

1. Introduction

Several A$_2$B$_2$O$_7$-based oxides, in particular doped La$_2$Ce$_2$O$_7$ (LCO), have been demonstrated in recent studies to have fairly good proton conductivity and to be robust in moist environments, making them a potential replacement for conventional materials used in SOFC devices.[1–7] In comparison to the electrolytes associated with Ba(Ce–Zr–Y)O$_3$, LCO bulk (pellet) has shown a range of sintering temperatures ranging from 1100 to 1300 °C. This represents a noteworthy reduction in sintering temperature in the free-standing pellet form. Therefore, there is a possibility of reduction of the processing temperature in SOFC devices using LCO.[2,8–11] The use of a lower processing/sintering temperature, nanomaterials, and new technologies has the potential benefit of lowering the expense of fuel cell manufacturing in addition to enhancing the electrochemical performance.[12–14] Nevertheless, when employing La$_2$Ce$_2$O$_7$ related electrolytes, the electrochemical performance is relatively low in comparison to Ba(Ce–Zr–Y)O$_3$ based electrolytes due to the lower proton conductivity.[7,15–19] New strategies are

necessary for the enhancement of proton conductivity while simultaneously ensuring the preservation of the chemical and thermal stability of newly doped La$_2$Ce$_2$O$_7$ materials. There are new challenges in predicting the structural phase of doped La$_2$Ce$_2$O$_7$ ceramics, which are known to be biphasic in nature (F-type and C-type phases), each with its own distinct ionic conducting behavior.[2,9] A number of elemental doping strategies were executed on LCO with the aim of enhancing its ionic conductivity with retained chemical stability.[7] Nonetheless, the investigations concerning the influence of the F/C phases and oxygen deficiencies on the ionic conductivity in these particular systems still lack clarity and demand further exploration to enable the engineering of material properties.

The LCO based materials have been reported to demonstrate exceptional catalytic activity for the oxidation coupling of methane within the intermediate temperature range of SOFCs.[7,20–23] Recently, Zhao *et al.*[24] reported the use of LCO and Sm-doped LCO (La$_{1.95}$Sm$_{0.05}$Ce$_2$O$_7$) as an internal reforming layer for methane, which was found to be stable in wet methane as compared to Sm-doped ceria. They proposed that when CH$_4$ was supplied, it first reaches the catalyst Ni–La$_{1.95}$Sm$_{0.05}$Ce$_2$O$_7$ layer, and undergoes water absorption and is converted into syngas before reaching the anode (Ni–Sm doped ceria). When compared with CH$_4$, syngas has been determined to possess superior carbon resistance and electroactivity. As a consequence, SOFCs with a catalytic layer of Ni$^+$ Sm-doped LCO display ameliorated electrochemical performance and stability in the presence

^{a} *Academy of Scientific and Innovative Research (AcSIR), Ghaziabad-201002, India.*
 E-mail: shahidanwr@gmail.com, shahid@immt.res.in, bishnumailg@gmail.com
^{b} *CSIR-Institute of Minerals and Materials Technology (IMMT), Bhubaneswar-751013, India*

of wet CH_4, in contrast to those without the catalyst layer. This study elucidates that doped LCO has the potential to serve as a viable candidate for a direct internal reforming layer. The direct use of doped LCO as an anode and a direct methane reforming layer without any extra layers may present a potential benefit for the advancement of SOFC technology. These potential benefits should be investigated to determine their stability in methane fuel to the anode made of doped LCO ceramics.

The thin coating of electrolyte on the anodic surface (anode supported cell) is a challenging endeavor that necessitates the utilization of an inexpensive and uncomplicated approach from a commercial standpoint. The anode supported electrolyte films based on LCO utilize the dry pressing method, which has been applied in most of the LCO-based SOFC studies.[1,8,25,26] However, this technique may pose challenges for larger SOFC production. The electrophoretic deposition of thin and compact electrolytes may be regarded as a cost-effective technology for SOFC industries.[27–29] Several classes of electrolyte material coatings utilizing EPD have been documented in the literature for the application of SOFCs.[29] A few attempts have been made towards the deposition of LCO-based electrolytes.[30–32] However, the investigation of EPD coatings for Yb-doped LCO has not been explored.

In this particular study, the synthesis of $La_{2-x}Yb_xCe_2O_7$ (where x values are 0, 0.05, 0.10, 0.15 and 0.20) nanoceramics was carried out by means of the glycine nitrate combustion route. A comprehensive study of the total ionic conductivity of the $La_{2-x}Yb_xCe_2O_7$ series was conducted, with significant emphasis on the contributions of the grain and grain boundary. The optimization of the thin film electrolyte coating of $La_{2-x}Yb_xCe_2O_7$ was achieved using EPD method. The resulting fuel electrode-supported SOFCs were fabricated using EPD, and their electrochemical performance was evaluated in the presence of wet hydrogen and wet methane at intermediate temperatures ranging from 700 to 500 °C (along with a short term stability test at 700 °C), with electrochemical reaction analysis being conducted using DRT analysis.

2. Experimental

$La_{2-x}Yb_xCe_2O_7$ (x = 0, 0.05, 0.10, 0.15 and 0.20) nanoceramics were synthesized through the employment of the glycine nitrate combustion route. The detailed procedure of the synthesis can be found in the cited literature.[9] The material compositions for $La_2Ce_2O_7$, $La_{1.95}Yb_{0.05}Ce_2O_7$, $La_{1.90}Yb_{0.10}Ce_2O_7$, $La_{1.85}Yb_{0.15}Ce_2O_7$, and $La_{1.80}Yb_{0.20}Ce_2O_7$ will be represented as LCO, Yb5, Yb10, Yb15, and Yb20, respectively, in the upcoming part of the paper. The phase and purity of the obtained powder (Rigaku, Ultima IV) were examined using the X-ray diffraction (XRD) technique using Cu Kα radiation with a wavelength of 0.15406 nm across a 2θ range of 20–80°. The synthesized powder was uniaxially pressed in a 15 mm strong steel die and sintered for 5 h at 1400 °C with a ramp rate of 3 °C min^{-1}. The study of the fluorite and C-type phases present in the $La_{2-x}Yb_xCe_2O_7$ series were analyzed using Raman spectroscopy.

The materials' Raman spectra were captured using a Renishaw InVia Raman spectrometer with a Renishaw RenCam CCD detector and an argon laser excitation source operating at 532 nm. The surface morphology was inspected using a scanning electron microscope (Carl Zeiss, SUPRA GEMINI55). An impedance analyzer (IM3570 impedance analyzer, Hikoi, Japan) was used to evaluate the ionic conductivity in moist oxygen ($\sim 3\%$ H_2O) from 200 to 700 °C with a signal amplitude of 100 mV. For improved current collection, the sintered electrolyte pellets were brush-coated with a silver paste. The silver paste was then heated at 250 °C for 2 h to evaporate the organics. Impedance spectra are matched with circuit components utilizing Zsimpwin software to glean information about the numerous electrochemical interactions. The anode composition was 60% NiO + 40% $La_{1.95}Yb_{0.05}Ce_2O_7$ + starch (20%). The process of electrophoretic deposition was fine-tuned to create a thin and impermeable coating of $La_{1.95}Yb_{0.05}Ce_2O_7$ electrolyte on the anode's surface to manufacture fuel electrode-supported SOFCs similar to the ref. 33. The article goes into detail about the various factors including the suspension chemistry that were improved to achieve the production of thin electrolyte films. After the fabrication of the thin film of $La_{1.95}Yb_{0.05}Ce_2O_7$ electrolyte followed by sintering at 1450 °C for 5 h, the cathode layer (70% LSCF–30% $La_{1.95}Yb_{0.05}Ce_2O_7$) was brush painted on the surface of the dense electrolyte to yield a complete fuel electrode-supported asymmetrical SOFC. High-temperature alumina adhesive paste was used to seal the SOFC devices onto an alumina tube. The electrochemical performances (I–V and impedance tests) of the cells were then evaluated using a CHI660E electrochemical workstation in a lab-made cell testing setup. The electrochemical performance of the cells was evaluated in the temperature range of 600–700 °C with wet H_2 and methane as the fuel and static air as the oxidant. DRT analysis was employed to scrutinize the fundamental electrochemical rate limiting mechanisms in the testing conditions of the SOFCs.

3. Results and discussion

3.1. Structural characterizations

The X-ray diffraction (XRD) spectra of the $La_{2-x}Yb_xCe_2O_7$ ceramics are presented in Fig. 1a. The diffraction pattern exhibits concurrence with the JCPDS card (JCPDS #04-12-6396), thereby indicating the presence of a distorted cubic fluorite phase. The absence of impurity peaks shows that all of the Yb has been completely doped to the La site. In order to conduct a thorough investigation into the effects of Yb doping, a close-up view of the (111) and (200) crystallographic plane is presented in Fig. 1b. When the smaller ionic radius of Yb^{3+}, measuring at 0.985 Å, is utilized to replace the larger La^{3+} ion with a radius of 1.16 Å, the resulting peak shift is observed towards higher angles. Ultimately, this phenomenon culminates in a reduction of the unit cell parameter shown in Fig. 1c. $La_{2-x}Yb_xCe_2O_7$ series crystallite sizes were observed to range from 9 to 15 nm on average. It should be emphasised,
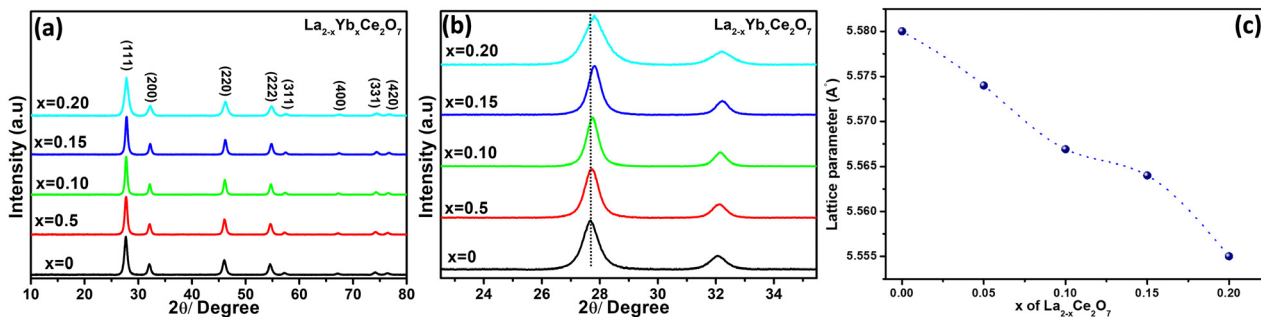
Fig. 1 (a) XRD pattern of the $La_{2-x}Yb_xCe_2O_7$ series calcined at 800 °C, (b) zoomed-in view of the (111) and (200) planes and (c) effect of lattice parameters on the doping of Yb.

nonetheless, that the C-type structure in the $La_{2-x}Yb_xCe_2O_7$ series, a crucial phase that influences the electrolyte's total ionic conductivity, is not revealed by the XRD peaks of LCO.[9] F and C type phases of $La_{2-x}Yb_xCe_2O_7$ are revealed by Raman spectroscopy in the next section.

In Fig. 2a, the pellets of the $La_{2-x}Yb_xCe_2O_7$ (normalized) Raman spectra are displayed. To examine the structural characteristics of the $La_{2-x}Yb_xCe_2O_7$ series, the peaks were deconvoluted using the Gaussian function to analyze the F and C-type phases. The intensity as well as area of the designated peaks were considered for calculation.[32] The Raman spectra typically show four strong peaks at about 578, 450, 361, and 254 cm^{-1}. The oxygen vacancy (O1) and F_{2g} are represented by the first two wide mode peaks at 578 and 450 cm^{-1}, respectively.[2,5,9,34] According to the ref. 2, 35 and 36, the oxygen vacancy (O2) and C-type phases are represented by the peaks at 361 and 254 cm^{-1}, respectively. According to certain sources,[34,37,38] the determination of the oxygen defect concentration in ceria-based materials can be explained by the area of peak O1 (578 cm^{-1}) and F_{2g} (450 cm^{-1}). In this study, the area of peak O1 ($\sim$578 cm^{-1}) and F_{2g} ($\sim$450 cm^{-1}) will be represented as (A_{575}/A_{445}). The ratio A_{575}/A_{445} exhibited a decreasing trend until $x = 0.10$. Subsequent doping of Yb (at $x = 0.15$ and 0.20) resulted in a very marginal increase, as depicted in Fig. 2b. This suggests that when Yb is

doped in LCO, the concentration of oxygen vacancies (O1) falls. The analysis of the oxygen vacancy (O1) peaks at 578 cm^{-1} holds important consideration; nonetheless, it is equally imperative to consider the peaks at 260 cm^{-1} (O2) owing to their connection with localized lattice distortions, which can facilitate in understanding the concentration and correlation of defects.[39] The calculation was conducted in order to investigate the impact of Yb doping on the 261 cm^{-1} and 578 cm^{-1} bands. The designated intensity ratio of O1 and O2, denoted as I_{260}/I_{575}, was utilized for this purpose. It was observed that the intensity ratio of I_{260}/I_{575} exhibited an initial increase until $x = 0.05$, followed by a subsequent decrease. However, it should be noted that the ratio I_{260}/I_{575} for compositions above $x = 0.05$ still remained higher than that of the pristine LCO, as illustrated in Fig. 2b. The observed data demonstrates that following the introduction of Yb, the band located at 261 cm^{-1} assumed a position of prominence, surpassing the band situated at 578 cm^{-1}. The biphasic character of Yb doped LCO can be discerned by employing the ratio of the intensity of the fluorite phase (F_{2g}) peak to the intensity of the C type phase (F/C phase). The F/C ratio of Yb-doped LCO has been computed and it has been observed that the F/C ratio increases until $x = 0.10$, after which the F/C phase ratio decreases (Fig. 2b). Such a modification in the phase composition may potentially impact the ionic conducting properties of the material.
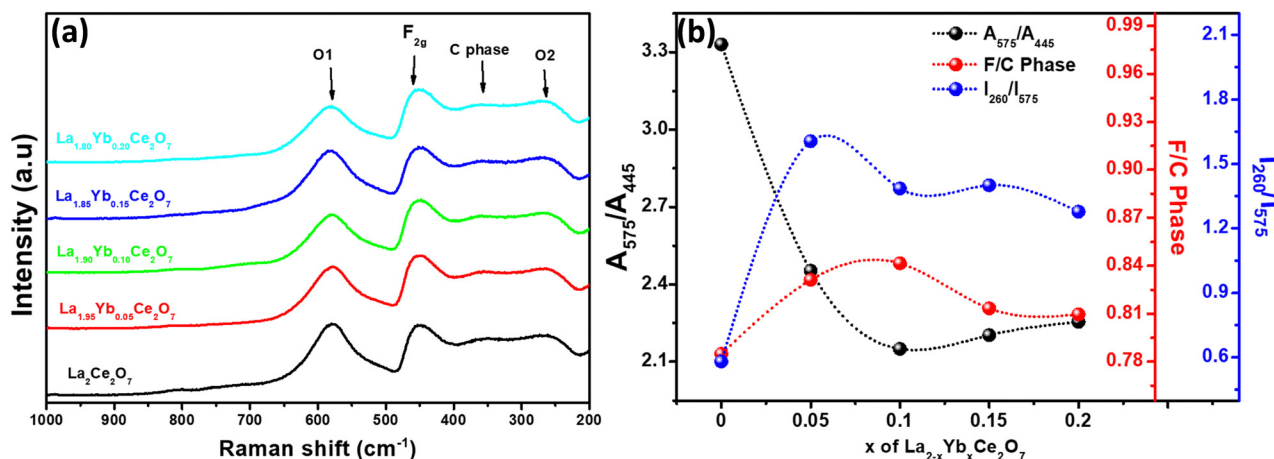

Fig. 2 (a) Normalized Raman spectra of $La_{2-x}Yb_xCe_2O_7$ pellets and (b) the effect of Yb doping on the ratio of (A_{575}/A_{445}), I_{260}/I_{575} and F/C phase.

3.2. Sintering studies

Pellets of $La_{2-x}Yb_xCe_2O_7$ were subjected to sintering in air at a temperature of 1400 °C for a duration of 5 h. The resulting microstructure of the pellets was analyzed through the use of SEM images, as illustrated in Fig. 3(a–e). The SEM images reveal that the $La_{2-x}Yb_xCe_2O_7$ pellets exhibit polygonal configurations, with a noticeably higher degree of densification in their surface morphologies, except for the $La_{1.80}Yb_{0.20}Ce_2O_7$ composition. In the case of the $La_{1.80}Yb_{0.20}Ce_2O_7$ composition (at $x = 20$), pores were observed in the microstructure, as shown in Fig. 3e. The determination of the average grain size was carried out through the utilization of ImageJ software. This involved a meticulous consideration of over 100 grains from the microstructures of each composition. Furthermore, as the Yb doping increases, the average grain size decreases, as seen in Fig. 3f. The decelerated diffusion mechanism that occurs across the grain boundaries during the process of sintering may be responsible for the reduction in mean grain sizes in Yb-doped LCO.[25,40] It was revealed in a recent work by Ishmil and Han[41] that the Yb doping of LCO ($La_2Ce_{1.9}Yb_{0.1}O_{7-\delta}$) caused the observation of pores in the microstructure. However, our materials are sintered at 1400 °C, which is 200 °C lower than theirs. They sintered the $La_2Ce_{1.9}Yb_{0.1}O_{7-\delta}$ at 1600 °C (produced *via* the solid-state approach).

3.3. Ionic conductivity of $La_{2-x}Yb_xCe_2O_7$ ceramics

The Nyquist plot for the $La_{1.95}Yb_{0.05}Ce_2O_7$ system at 700 °C is effectively depicted in Fig. 4, serving as a representative image. The Nyquist plots of the $La_{2-x}Yb_xCe_2O_7$ series were fitted using the circuit element $(RQ)(RQ)(RQ)$, with R representing resistance and Q representing a constant phase element (CPE). The following equation is used to calculate total ionic
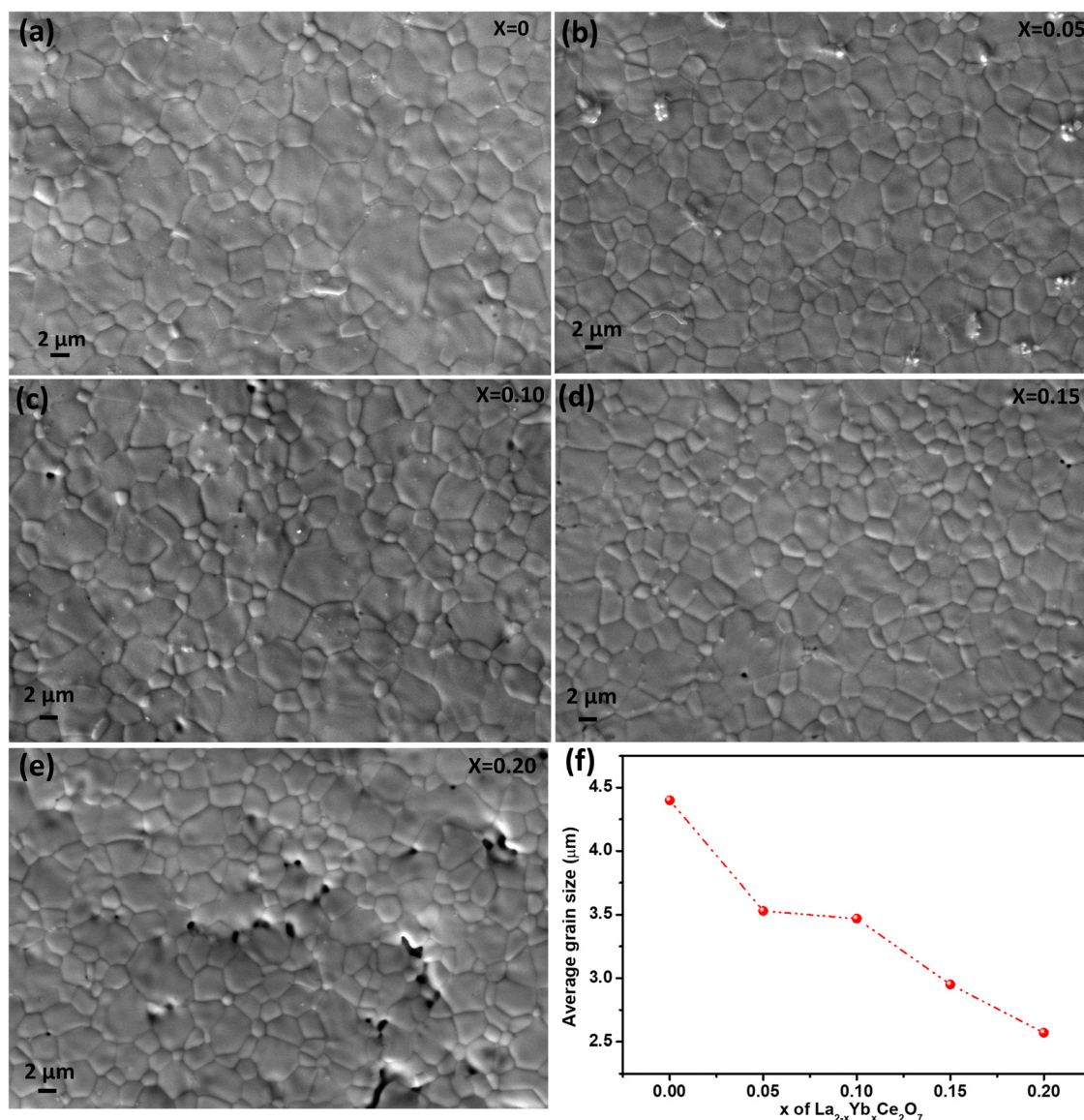

Fig. 3 (a)–(e) Surface morphology of $La_{2-x}Yb_xCe_2O_7$ pellets sintered at 1400 °C for 5 h and (f) average grain size against Yb doping level for the LCO.
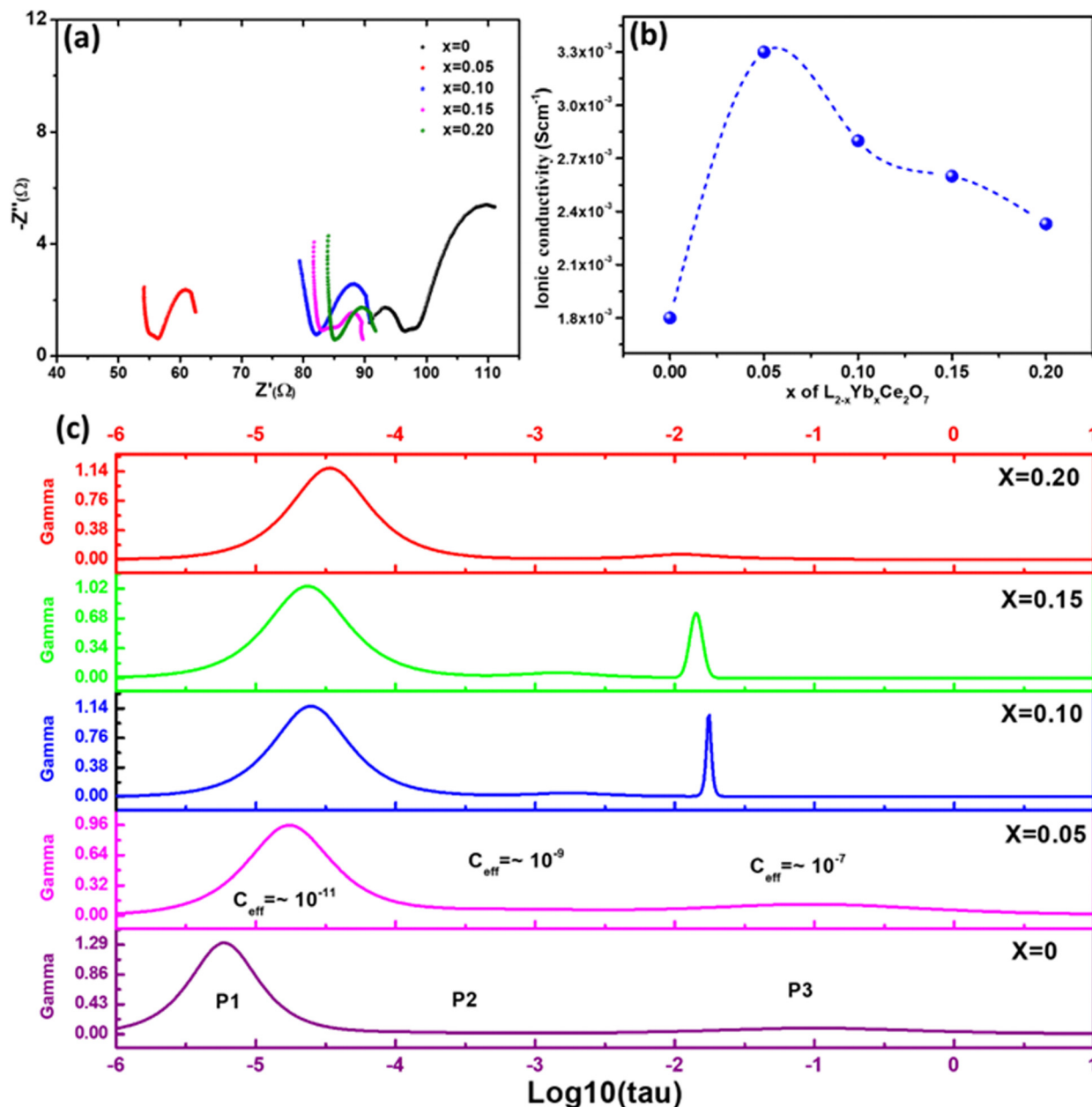
Fig. 4 (a) Impedance spectra of the $La_{2-x}Yb_xCe_2O_7$ series in moist oxygen at 700 °C, (b) effect of Yb doping on ionic conductivity and (c) ISGP spectra of the $La_{2-x}Yb_xCe_2O_7$ series at 300 °C.

conductivity:

$$\sigma = \frac{L}{AR} \qquad (1)$$

where σ is the total ionic conductivity, A is the surface area of the silver paint, L is the thickness of the electrolyte, and R is the total resistance. All Yb-doped $La_2Ce_2O_7$ ceramics had higher conductivities than undoped $La_2Ce_2O_7$ samples in wet oxygen. For $x = 0$, 0.05, 0.10, 0.15, and 0.20, the total ionic conductivity determined at 700 °C was 1.8×10^{-3} S cm^{-1}, 3.3×10^{-3} S cm^{-1}, 2.8×10^{-3} S cm^{-1}, 2.6×10^{-3} S cm^{-1}, and 2.33×10^{-3} S cm^{-1}. The findings demonstrate that, when compared to $La_2Ce_2O_7$, $La_{2-x}Yb_xCe_2O_7$ electrolyte has greater electrical conductivity

under the test conditions, with $La_{1.95}Yb_{0.05}Ce_2O_7$ exhibiting the best ionic conductivity. It is imperative to bear in mind that the area ratio A_{575}/A_{445} served as a consequential measure of oxygen vacancy concentrations in doped ceria systems. It was interesting to notice that, in accordance with Fig. 2b, subsequent to Yb doping to the LCO lattice, the area ratio of A_{575}/A_{445} was evinced to be decreasing while the intensity ratio of I_{260}/I_{575} was established to be higher than that of the undoped LCO and the maximal intensity ratio I_{260}/I_{575} was observed at $x = 0.05$, after which it decreased at higher x (i.e., $x > 0.05$). The peak of approximately 260 cm^{-1}, which was identified as an oxygen vacancy (O2), must have thus contributed to the ionic conductivity of the Yb-doped $La_2Ce_2O_7$ ceramics. The lower ionic

conductivity in the higher amount of Yb may be caused by the intrinsic conductivity of the grain boundaries. To comprehend the contribution of the grain boundary, the space charge potential was calculated using the distribution function of relaxation time (DFRT) using impedance spectroscopy genetic programming (ISGP). When compared to Impedance spectroscopy spectra, the ISGP can clearly and precisely differentiate the contribution from the grain and grain boundary.[42–44] Following the investigation of grain and grain boundary conductivity using ISGP, the Mott–Schottky space charge layer model was employed to examine the barrier height at the grain boundary core as per the following eqn (2).[45] The capacitance values of peak P1, P2 and P3 were determined to be approximately $\sim 10^{-11}$, 10^{-9} and 10^{-8} to 10^{-7} F cm^{-2}, respectively, corresponding to the grain interior, grain boundary and electrode,[43,45,46] as indicated in Fig. 4c. The visibility of the P2 peak of $x = 0.05$ is not readily apparent in Fig. 4c due to the extensive frequency range. Nevertheless, it is perceptible in the low frequency range, as demonstrated in Fig. S1 (ESI†).

$$\frac{\tau_{gb}}{\tau_g} = \frac{e^{\frac{q\phi(0)}{k_B T}}}{2\frac{q\phi(0)}{k_B T}} \qquad (2)$$

where, τ_{gb}, τ_g, e, k_B, T and $\Phi(0)$ are the relaxation time constant of the grain boundary, grains, electronic charge, Boltzmann constant, temperature and grain boundary core potential (potential barrier height), respectively. The grain boundaries physically face the oxide ion or proton conduction channel. The grain boundary conductivity having a value that is many orders of magnitude lower than the bulk grain conductivity illustrates the grain boundary blocking 'intrinsic' impact. The blocking effect can be caused by lattice mismatch, dislocations, flaws, *etc.*[47–49] As shown in Fig. 5b, the conducting ions must cross a minimal obstruction known as the potential barrier height. The change in $\Phi(0)$ with varying Yb contents at 300 °C is depicted in Fig. 5(c). At $x = 0$, 0.05, 0.10, 0.15, and 0.20, the values of $\Phi(0)$ at 300 °C were determined to be around 0.36, 0.27, 0.33, 0.34, and 0.42 V, respectively. In comparison to other compositions, the lower $\Phi(0)$ shows that $x = 0.05$ is more conducive to protons being transported across the electrolyte grain boundary.

The results of this investigation show, however, that Yb in LCO at greater doping levels ($x > 0.05$) exhibits an intrinsic grain boundary proton blocking effect. The potential values of the grain boundary core in the La$_{2-x}$Yb$_x$Ce$_2$O$_7$ series at a temperature of 300 °C exhibit a clear correlation with the observed trends in both total ionic conductivity and Raman spectroscopy results. Therefore, the incorporation of Yb dopants into LCO (at $x = 0.05$) yields a noteworthy reduction in the potential barrier height at the grain boundary core. It has been reported in the literature that there exists a comparable potential barrier height at the grain boundary core for proton conducting electrolytes related to BZCY.[50,51]

3.4. EPD of La$_{1.95}$Yb$_{0.05}$Ce$_2$O$_7$ powders

Among the ceramics of La$_{2-x}$Yb$_x$Ce$_2$O$_7$, the highest ionic conductivity is exhibited by La$_{1.95}$Yb$_{0.05}$Ce$_2$O$_7$ (at $x = 0.05$). Consequently, it was ultimately selected as the preferred electrolyte for the fabrication of SOFCs. The EPD methodology was employed to produce a thin and compact electrolyte layer on the fuel electrode. To prepare the suspension of La$_{1.95}$Yb$_{0.05}$Ce$_2$O$_7$, a 2 wt% La$_{1.95}$Yb$_{0.05}$Ce$_2$O$_7$ powder was dispersed in acetylacetone, ethanol, isopropanol, butanol, and acetone. These suspensions were labelled as 1, 2, 3, 4, and 5, respectively, as illustrated in Fig. 6. After a duration of 69 h, the suspensions were evaluated for stability, and it was observed that isopropanol exhibited the highest stability, followed by butanol, ethanol, acetylacetone, and finally acetone (as shown in Fig. 6d). The particle size distribution of the La$_{1.95}$Yb$_{0.05}$Ce$_2$O$_7$ suspension in isopropanol is shown in Fig. 6e. The EPD of La$_{1.95}$Yb$_{0.05}$Ce$_2$O$_7$ was performed in isopropanol (mean zeta potential = +41.7 mV) by varying the deposition parameters (electrode distance: ~ 1.5 cm, time: 45 s to 6 min; and voltage: 40 to 60 V). It was found that 50 V for 4 min of deposition was the ideal deposition condition followed by 5 h of sintering at 1450 °C. The resultant La$_{1.95}$Yb$_{0.05}$Ce$_2$O$_7$ film coated by EPD in isopropanol was observed to possess a thin, crack-free, and dense structure. The subsequent section of the paper shall elucidate upon the microstructure of the film. Additional details concerning the preparation and processing of the suspension may be obtained from the ESI.†
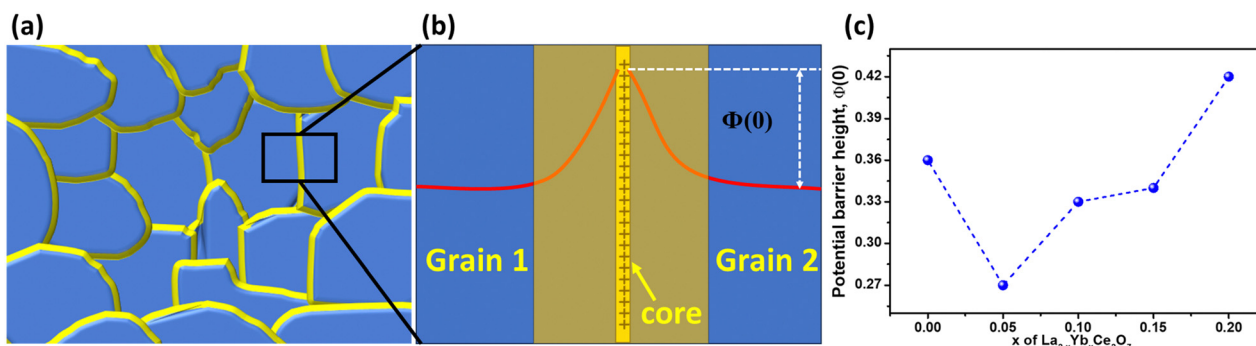

Fig. 5 (a) and (b) Schematic representation of the grains and grain boundary with certain potential barrier height and (c) effect of Yb doping on the potential barrier height of La$_{2-x}$Yb$_x$Ce$_2$O$_7$ ceramics at 300 °C.
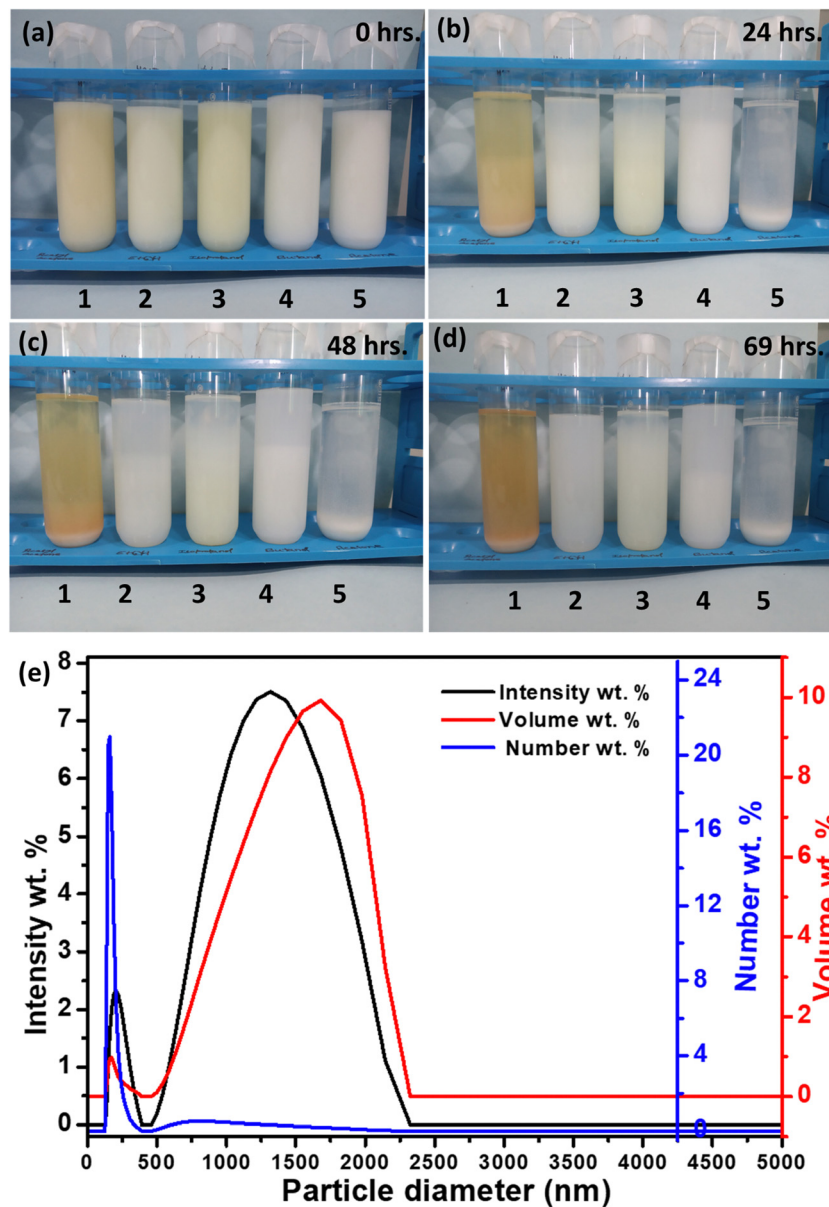
Fig. 6 (a)–(d) Suspension stability test of $La_{1.95}Yb_{0.05}Ce_2O_7$ powder in different media at different time intervals and (e) particle size distribution curve of $La_{1.95}Yb_{0.05}Ce_2O_7$ powder in isopropanol media.

3.5. Microstructure and electrochemical performance

The thickness of the cell's components was calculated to be approx. 35, 14, and 800 μm for the cathode, electrolyte, and anode, respectively. The microstructure of the tested cell (after testing in methane and hydrogen fuel and stability test) is shown in Fig. 7a. After sintering at 1450 °C for 5 h, the electrophoretically deposited $La_{1.95}Yb_{0.05}Ce_2O_7$ electrolyte was dense and adherent to the anode, as illustrated in Fig. 7a. The interface between anode and electrolyte is depicted in the inset image of Fig. 7a (right side), demonstrating that no cracks or delamination were observed following testing in both H_2 & CH_4 fuels, as well as short-term stability testing. Similarly, it was observed that the interface existing between the cathode and electrolyte was devoid of any cracks, as can be seen from the left inset image of Fig. 7a.

Nonetheless, it is evident that the cathode layer was not entirely integral to the electrolyte layer (Fig. S3, ESI†). Thus, it can be observed that the triple phase boundary (TPB) existing between the cathode and electrolyte is comparatively less as compared to the TPB existing between the anode and electrolyte. The porosity calculated from the microstructure of the cathode (Fig. 7b) was approx. 28%. Fig. 7c depicts the elemental line mapping of the evaluated cell. Notably, no new phases or elemental reactions occurred during the course of the testing or sintering during cell fabrication. In addition, reactivity between the NiO and $La_{1.95}Yb_{0.05}Ce_2O_7$ (after sintering at 1450 °C for 5 h) was also checked using XRD. Fig. 7d clearly illustrates that the distinct phase of $La_{1.95}Yb_{0.05}Ce_2O_7$ and cubic NiO phase (JCPDS 47-1049) were formed without any reactions between them.
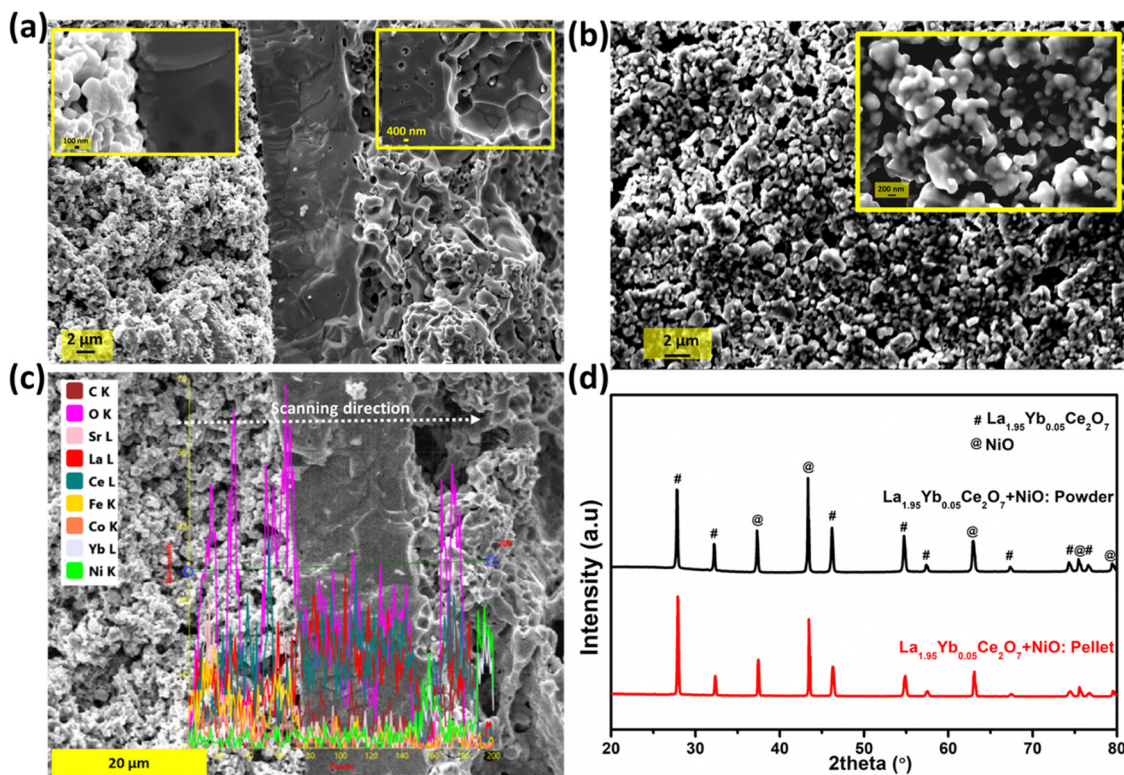
Fig. 7 (a) Cross-section microstructure of the tested cell [left inset: cathode & electrolyte interface, right inset: electrolyte & anode interface]; (b) microstructure of the cathode (inset: magnified image), (c) EDX elemental cross-sectional line scanning of the tested cell and (d) XRD of anode composite (NiO+ La$_{1.95}$Yb$_{0.05}$Ce$_2$O$_7$) after sintering at 1450 °C.

The electrochemical behavior of the cell was evaluated within the temperature spectrum of 500–700 °C, utilizing a moist hydrogen fuel with a water content of approximately 3%, while static air was employed as the oxidizing agent. The maximum power density (MPD) generated by cell [Ni–La$_{1.95}$Yb$_{0.05}$Ce$_2$O$_7$ (anode)//La$_{1.95}$Yb$_{0.05}$Ce$_2$O$_7$ (electrolyte)//LSCF + La$_{1.95}$Yb$_{0.05}$Ce$_2$O$_7$ (cathode)] was 589, 505, 363, 202 and 90 mW cm^{-2} at 700, 650, 600, 550, and 500 °C, respectively. The MPD of this study is well comparable with the LCO and BZCY-based electrolyte.[5,26,50,52–54] This research demonstrates enhancement in MPD when compared to the La$_{1.85}$Y$_{0.15}$Ce$_2$O$_7$ electrolyte-based SOFC.[31] However, it should be noted that some literatures have reported high performances, which are based on doped LCO; for example, Zhang *et al.*[1] achieved the MPD of 1031 mW cm^{-2} at 700 °C and Wu *et al.*[8] reported the MPD of 897 mW cm^{-2} at 700 °C by utilizing La$_{1.85}$Mg$_{0.15}$Ce$_2$O$_{7-\delta}$ electrolyte.

Under the testing conditions for the fuel cell, the open circuit voltage (OCV) obtained was recorded as 0.866, 0.89, 0.915, 0.927 and 0.927 V at temperatures of 700, 650, 600, 550, and 500 °C, respectively. The present study reveals an observed improvement in the OCV value when high-performance devices are compared.[1,8] However, the potential for further enhancement of OCV exists through anode composition modification. As an example, Ling *et al.*[53] have demonstrated an increase in OCV from 0.92 V to 1.0 V through the utilization of NiO–BaZr$_{0.1}$Ce$_{0.7}$Y$_{0.2}$O$_{3-\delta}$ as an anode instead of NiO–LCO. This improvement was attributed to the development of a proton

conducting phase at the interface between the anode and electrolyte, which represents a promising area for future study. However, these OCV values were found to be lower than the theoretical values. This discrepancy is attributed to the electronic leakage in the LCO-based electrolytes, which occurs due to the reduction of Ce^{4+} to Ce^{3+} under reducing atmospheres.[7] This suggested that a rise in the temperature of the testing medium results in a decline in ionic transportation. This decrease can be attributed to the higher mobility of holes and proton dehydration in the structure.[50] This phenomenon also extends a possible explanation for the decrease in the OCV value. We performed an EIS of the cell under OCV conditions to isolate the resistance contribution (ohmic resistance, R_o; polarization resistance, R_P) in the constructed cell. The EIS of the cell tested in the 500–700 °C range is shown in Fig. 8b. The cell's R_o was calculated to be 0.28, 0.32, 0.40, 0.59, and 1.33 Ω cm^2 at 700, 650, 600, 550, and 500 °C, respectively, while the R_P was calculated to be 0.82, 0.76, 0.43, 0.62, and 1.14 Ω cm^2 at 700, 650, 600, 550, and 500 °C, respectively. It was strange to note that R_P calculated at 700 and 650 °C was higher than that calculated at 600 and 550 °C. From EIS, the size of the low frequency arc was higher (at 700 and 650 °C), as shown in Fig. S4 (ESI†). The observed phenomenon may be attributed to the destabilization of the cell and electronic leakage in the electrolyte at elevated operating temperatures, specifically at 700 and 650 °C.[32] Nevertheless, it is noteworthy that the cell may exhibit stability over prolonged operation, as evidenced by the findings of DiGiuseppe,[55] who reported a great reduction in
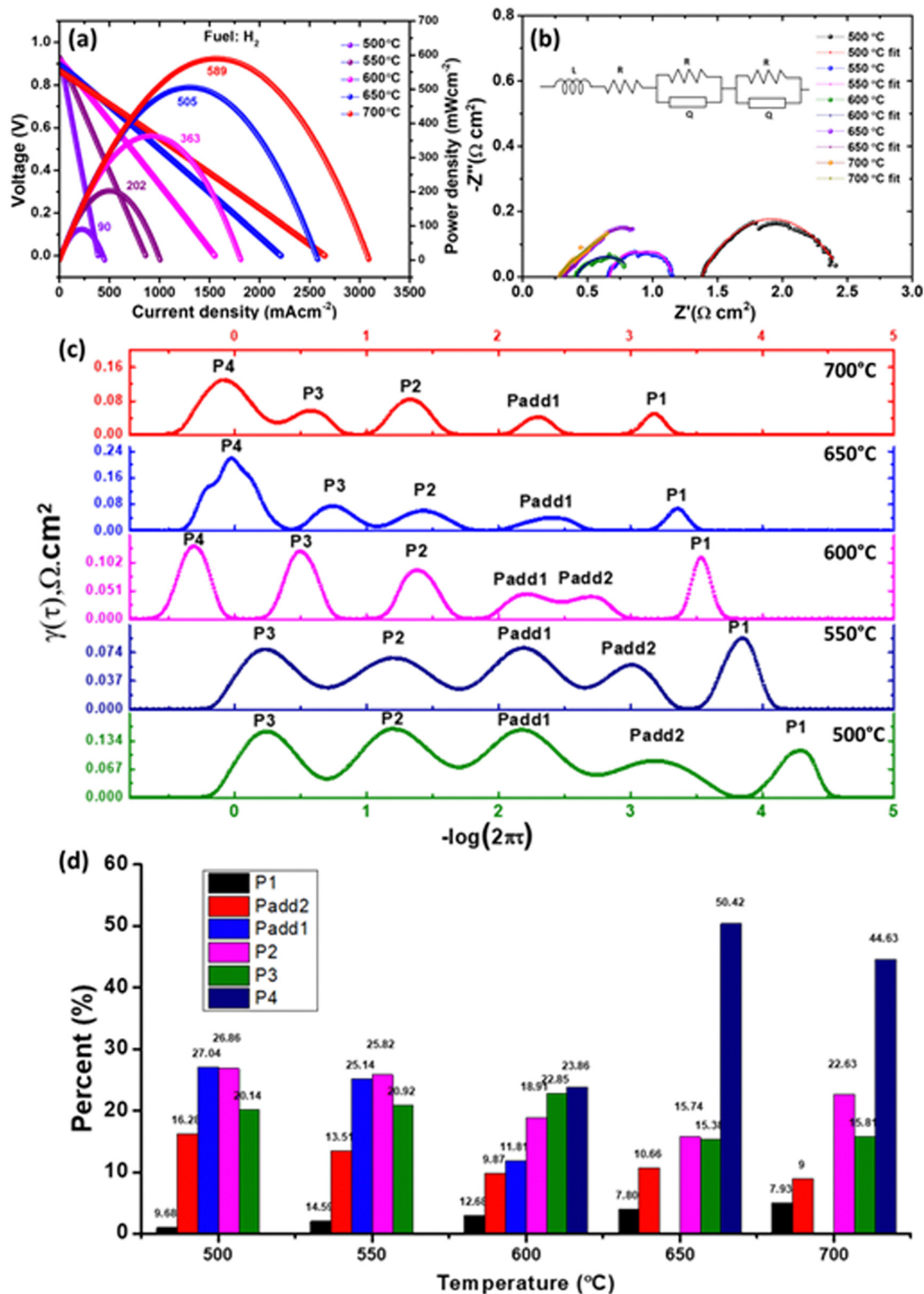
Fig. 8 (a) $I-V-P$ plot of the cell in the moist H_2 fuel ($\sim$3% H_2O), (b) impedance spectra plot of the cells measured at various temperatures, (c) corresponding DRT analysis of the cell and (d) percentage of the polarization resistance in the DRT analysis.

the polarization resistance of LSCF-based cathode after a duration of 1050 h. Furthermore, in order to comprehensively comprehend the polarization contribution of the electrodes in the cell with utmost precision, the utilization of the distribution of relaxation

time (DRT) method was implemented.[56,57] Fig. 8c depicts the DRT curves that were obtained from the impedance spectroscopy data within the temperature range of 500–700 °C. The four peaks found on the DRT curves were labelled as P1–P4 (from high to low

frequency). Each peak functions as an indicator of the rate-limiting steps in the electrode reactions, and every peak manifests a distinct variation tendency at diverse testing temperatures. The peak denoted as P1 and Padd2 is fundamentally associated with

the anode reactions encompassing hydrogen absorption, dissociation, proton formation, and proton assimilation into the lattice of the electrolyte.[6,58] The peak P1 and Padd2 moves to a lower frequency as the testing temperature rises, indicating that the

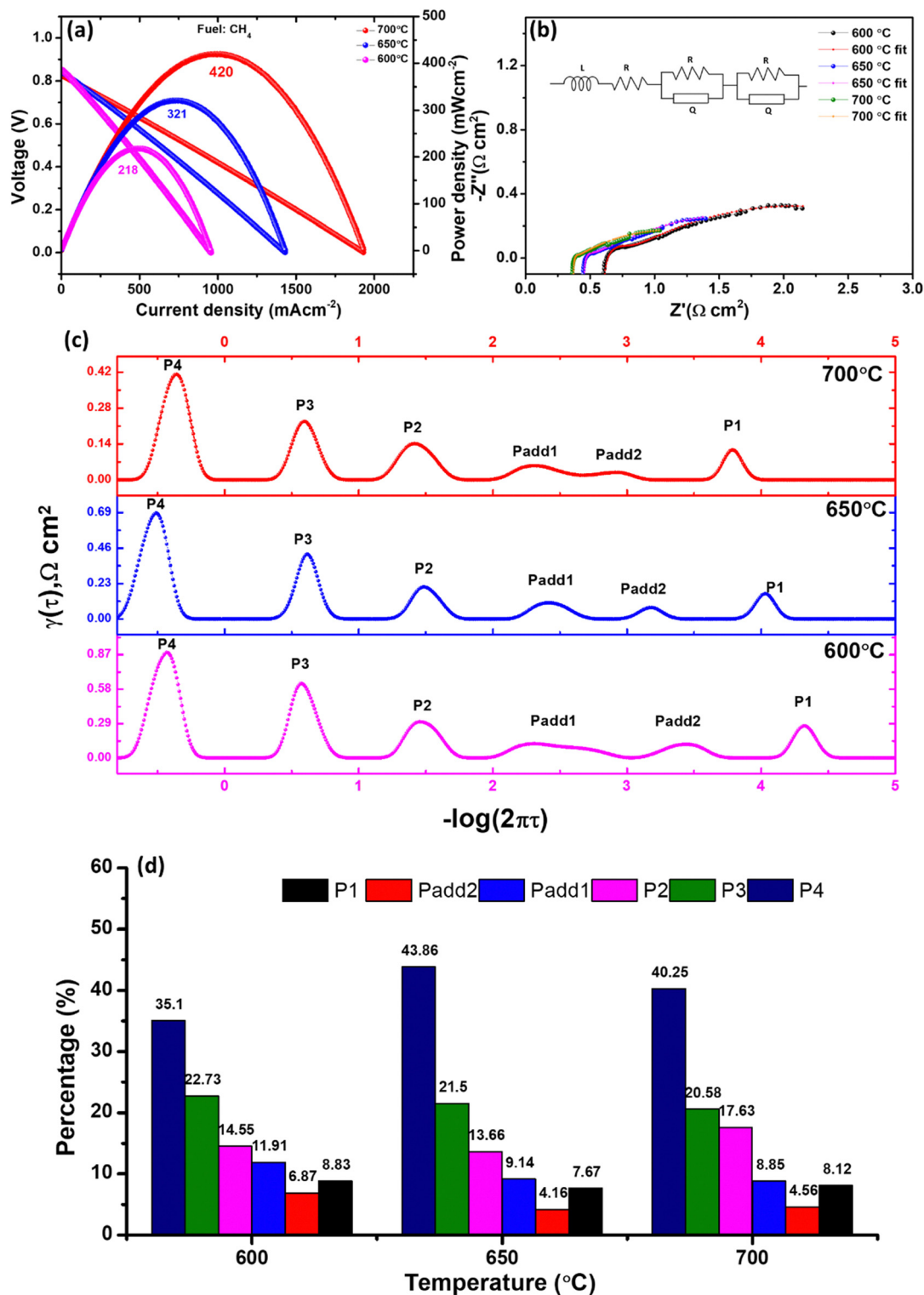Fig. 9 (a) $I–V–P$ plot of the cell in the moist CH_4 fuel ($\sim 3\%$ H_2O), (b) impedance spectra plot of the cells measured at various temperatures, (c) corresponding DRT analysis of the cell and (d) percentage of polarization resistance in the DRT analysis.

process is thermally active. However, Padd2 disappeared from 650 to 700 °C. The incorporation of O^{2-} in the electrolyte lattice, as evidenced by all DRT curves, could potentially be denoted by Padd1.[58] P2 depicts the process of proton diffusion in the cell's air electrode, P3 represents gas diffusion to the anodic and cathodic parts of the cell, and P4 may show the illustrated polarization owing to anodic gas diffusion.[6] It is noteworthy to observe that P4 is observed at elevated temperatures. This is attributed to the electrolyte's alteration towards oxide ion dominance over protons beyond the threshold of 600 °C. Consequently, fuel dilution phenomena manifest. From the data presented in Fig. 8d, it is noteworthy to observe that the anodic polarization (P4) resistance was found to be the predominant factor contributing towards the cell's performance above 600 °C of operation. However, it is important to mention that the combined effect of P1 and Padd1 was responsible for nearly half of the overall polarization resistance.

To the best of our knowledge, we are reporting for the first time the utilization of an LCO-based anode in CH_4 fuel. The MPD of the cell, as depicted in Fig. 9a, was determined through the utilization of moist methane as a fuel. The MPD values were calculated at different temperatures, namely 700 °C, 650 °C, and 600 °C, and were found to be 420, 321, and 218 mW cm^{-2}, respectively. Also, the OCV values were evaluated at the same temperatures and amounted to 0.83, 0.84, and 0.85 V, respectively. The MPD exhibited in this study can be compared to that of proton conducting SOFCs.[58–60] However, there are other studies that have demonstrated high performance in methane fuel. For instance, Konwar et al.[61,62] have reported an MPD exceeding 800 mW cm^{-2} at 600 °C, while Duan et al.[17] have reported a power density exceeding 300 mW cm^{-2} at the same temperature. It is noteworthy that the aforementioned investigations were conducted under conditions of reduced methane concentration or with the inclusion of an extra catalyst layer to augment performance and mitigate coking; however, in our experimentation, no supplementary catalyst layer was incorporated. Apart from Ni in the anode, $La_{1.95}Yb_{0.05}Ce_2O_7$ is believed to be an excellent catalyst for methane according to the study performed by Zhao et al.[24] The R_o of the cell from the impedance spectra (Fig. 9b) was calculated to be 0.358, 0.43 and 0.57 Ω cm^2 at 700, 650, and 600 °C, respectively, whereas R_p was

calculated to be 1.52, 2.66 and 2.88 Ω cm^2 at 700, 650, and 600 °C, respectively. The DRT spectra are shown in Fig. 9c. Here, internal reforming of methane was taking place at the fuel electrode to produce syngas according to the following equations:

$$CH_4 + 2H_2O \rightarrow CO_2 + 4H_2 \quad (3)$$

$$CH_4 + H_2O \rightarrow CO + 3H_2 \quad (4)$$
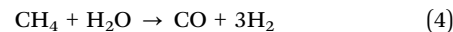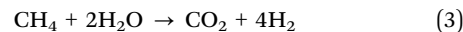
The DRT curves at 700 °C (tested in both fuel H_2 and CH_4) are compared in the Fig. S5 (ESI†). It is evident from the results that the peak P1 of methane fuel has shifted towards higher frequency, which is indicative of the anodic reactions being sluggish. Furthermore, in the moist H_2 fuel, it was observed that Padd2 did not serve as the rate limiting step at 700 °C.

An additional rate limiting step was formed Padd1 (Padd1 splits from 650 °C) in DRT at 600 °C. Fig. 9d illustrates the polarization resistance in percentage and it can be noticed that almost 50% of the polarization contribution was from electrode gas diffusion processes. Therefore, engineering the interface along with the catalyst layer (externally or internally) on the cell is a futuristic study to reduce the electrode gas diffusion resistance.

The short-term stability test was carried out in moist hydrogen at 700 °C, as illustrated in Fig. 10. Initially, the cell appears to be stable for up to 12 h with a steady current density (482 mA cm^{-2}). After 12 h, the current density drops from 482 to 475 mA cm^{-2}, and after 30 h, the current density drops to 458 mA cm^{-2}. At 700 °C, the electrochemical performance dropped by 5% after 30 h of operation.

4. Conclusions

The crystal structure and phases present in the Yb-doped $La_2Ce_2O_7$ were studied extensively using X-ray diffraction and Raman spectroscopy to reveal its dual phase character F-type and C-type phase. Doping affects the dual phases in the system. The ionic conductivity and space charge potential of the Yb-doped $La_2Ce_2O_7$ were studied and at $x = 0.05$ it showed the highest ionic conductivity of 3.3×10^{-3} S cm^{-1} at 700 °C.
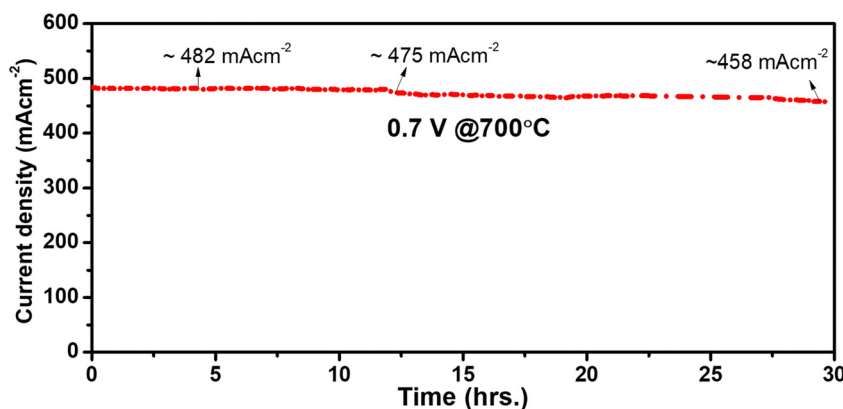
Fig. 10 Short-term stability test in moist hydrogen at 700 °C.

     © 2024 The Author(s). Published by the Royal Society of Chemistry

The La$_{1.95}$Yb$_{0.05}$Ce$_2$O$_7$ film coated by EPD in isopropanol was established with a crack-free and dense coating with a thickness of approx. 14 μm. The MPDs in hydrogen fuel generated by the cell were 589, 505, 363, 202 and 90 mW cm^{-2} at 700, 650, 600, 550, and 500 °C, respectively. In moist methane as a fuel, the MPD reached a value of 420, 321, and 218 mW cm^{-2} at 700, 650, and 600 °C, respectively. DRT analysis using Impedance spectra analysis suggests that the gas diffusion process in the electrodes contributes greatly to the total polarization of the cell. Therefore, the manipulation of the interface coupled with the catalyst layer (either externally or internally) on the cell is a prospective area of research aimed at mitigating the resistance to the diffusion of electrode gases.

Conflicts of interest

There are no conflicts to declare.

Acknowledgements

References

1 M. Zhang, D. Wang, L. Miao, Z. Jin, K. Dong and W. Liu, *Electrochem. Commun.*, 2021, 107026.

2 J. Zamudio-Garcia, L. dos Santos-Gomez, J. M. Porras-Vázquez, E. R. Losilla and D. Marrero-Lopez, *J. Alloys Compd.*, 2020, **816**, 152600.

3 W. Sun, S. Fang, L. Yan and W. Liu, *Fuel Cells*, 2012, **12**, 457–463.

4 S. A. Ismail, L. Jiang, P. Zhong, T. Norby and D. Han, *J. Alloys Compd.*, 2022, **899**, 163306.

5 T. Tu, B. Zhang, J. Liu, K. Wu and K. Peng, *Electrochim. Acta*, 2018, **283**, 1366–1374.

6 X. Wang, Z. Ma, T. Zhang, J. Kang, X. Ou, P. Feng, S. Wang, F. Zhou and Y. Ling, *ACS Appl. Mater. Interfaces*, 2018, **10**, 35047–35059.

7 B. Choudhary, L. Besra, S. Anwar and S. Anwar, *Int. J. Hydrogen Energy*, 2023, **48**, 28460–28501.

8 Y. Wu, Z. Gong, J. Hou, L. Miao, H. Tang and W. Liu, *Int. J. Hydrogen Energy*, 2019, **44**, 13835–13842.

9 B. Choudhary, S. Anwar, D. A. Medvedev, L. Besra and S. Anwar, *Ceram. Int.*, 2022, **48**, 6758–6766.

10 J. Li, C. Wang, X. Wang and L. Bi, *Electrochem. Commun.*, 2020, **112**, 106672.

11 F. J. A. Loureiro, N. Nasani, G. S. Reddy, N. R. Munirathnam and D. P. Fagg, *J. Power Sources*, 2019, **438**, 226991.

12 Z. Cao, L. Fan, G. Zhang, K. Shao, C. He, Q. Zhang, Z. Lv and B. Zhu, *Catal. Today*, 2019, **330**, 217–221.

13 L. Yu, J. Huang, Y. Li, Y. Jing, K. Maliutina, R. Ma and L. Fan, *Ceram. Int.*, 2021, **47**, 16956–16963.

14 L. Fan, B. Zhu, P.-C. Su and C. He, *Nano Energy*, 2018, **45**, 148–176.

15 W. Bian, W. Wu, B. Wang, W. Tang, M. Zhou, C. Jin, H. Ding, W. Fan, Y. Dong, J. Li and D. Ding, *Nature*, 2022, **604**, 479–485.

16 Z. Tao, M. Fu, Y. Liu, Y. Gao, H. Tong, W. Hu, L. Lei and L. Bi, *Int. J. Hydrogen Energy*, 2022, **47**, 1947–1953.

17 C. Duan, R. J. Kee, H. Zhu, C. Karakaya, Y. Chen, S. Ricote, A. Jarry, E. J. Crumlin, D. Hook and R. Braun, *Nature*, 2018, **557**, 217–222.

18 L. Yang, S. Wang, K. Blinn, M. Liu, Z. Liu, Z. Cheng and M. Liu, *Science*, 2009, **326**, 126–129.

19 Z. Zhu, B. Liu, J. Shen, Y. Lou and Y. Ji, *J. Alloys Compd.*, 2016, **659**, 232–239.

20 J. Xu, Y. Zhang, X. Xu, X. Fang, R. Xi, Y. Liu, R. Zheng and X. Wang, *ACS Catal.*, 2019, **9**, 4030–4045.

21 J. Xu, L. Peng, X. Fang, Z. Fu, W. Liu, X. Xu, H. Peng, R. Zheng and X. Wang, *Appl. Catal., A*, 2018, **552**, 117–128.

22 J. Wang, F. Liu, J. Wu, S. Zou and J. Fan, *Catal. Sci. Technol.*, 2023, **13**, 2493–2499.

23 R. Singh Pal, S. Rana, S. Kumar Sharma, R. Khatun, D. Khurana, T. Suvra Khan, M. Kumar Poddar, R. Sharma and R. Bal, *Chem. Eng. J.*, 2023, **458**, 141379.

24 J. Zhao, X. Xu, W. Zhou, I. Blakey, S. Liu and Z. Zhu, *ACS Appl. Mater. Interfaces*, 2017, **9**, 33758–33765.

25 B. Zhang, Z. Zhong, T. Tu, K. Wu and K. Peng, *J. Power Sources*, 2019, **412**, 631–639.

26 T. Tu, J. Liu and K. Peng, *Ceram. Int.*, 2017, **43**, 16384–16390.

27 S. Hu, W. Li, H. Finklea and X. Liu, *Adv. Colloid Interface Sci.*, 2020, **276**, 102102.

28 L. Besra and M. Liu, *Prog. Mater. Sci.*, 2007, **52**, 1–61.

29 E. Y. Pikalova and E. Kalinina, *Renewable Sustainable Energy Rev.*, 2019, **116**, 109440.

30 B. Choudhary and S. Anwar, *Solid State Ionics*, 2023, **401**, 116356.

31 B. Choudhary, K. S. Dash, S. Anwar, L. Besra and S. Anwar, *J. Power Sources*, 2023, **583**, 233543.

32 B. Choudhary and S. Anwar, *ACS Appl. Energy Mater.*, 2023, **6**, 11817–11827.

33 B. Choudhary, S. Anwar, L. Besra and S. Anwar, *Int. J. Appl. Ceram. Technol.*, 2019, **16**, 1022–1031.

34 Y. Xu, F. Wang, X. Liu, Y. Liu, M. Luo, B. Teng, M. Fan and X. Liu, *J. Phys. Chem. C*, 2019, **123**, 18889–18894.

35 K. Singh, R. Kumar and A. Chowdhury, *Ultrason. Sonochem.*, 2017, **36**, 182–190.

36 A. Nakajima, A. Yoshihara and M. Ishigame, *Phys. Rev. B: Condens. Matter Mater. Phys.*, 1994, **50**, 13297–13307.

37 Z.-Y. Pu, X.-S. Liu, A.-P. Jia, Y.-L. Xie, J.-Q. Lu and M.-F. Luo, *J. Phys. Chem. C*, 2008, **112**, 15045–15051.

38 Z.-Y. Pu, J.-Q. Lu, M.-F. Luo and Y.-L. Xie, *J. Phys. Chem. C*, 2007, **111**, 18695–18702.

39 R. Schmitt, A. Nenning, O. Kraynis, R. Korobko, A. I. Frenkel, I. Lubomirsky, S. M. Haile and J. L. M. Rupp, *Chem. Soc. Rev.*, 2020, **49**, 554–592.

40 M. Amsif, D. Marrero-Lopez, J. C. Ruiz-Morales, S. N. Savvin, M. Gabás and P. Nunez, *J. Power Sources*, 2011, **196**, 3461–3469.

41 S. A. Ismail and D. Han, *J. Am. Ceram. Soc.*, 2022, **105**, 7548–7557.

42 S. Hershkovitz, S. Baltianski and Y. Tsur, *Solid State Ionics*, 2011, **188**, 104–109.

43 T. Paul, N. Yavo, I. Lubomirsky and Y. Tsur, *Solid State Ionics*, 2019, **331**, 18–21.

44 T. Paul and Y. Tsur, *Solid State Ionics*, 2018, **323**, 37–43.

45 A. K. Baral and Y. Tsur, *Solid State Ionics*, 2017, **304**, 145–149.

46 A. K. Baral and Y. Tsur, *J. Am. Ceram. Soc.*, 2019, **102**, 239–250.

47 D. R. Clark, H. Zhu, D. R. Diercks, S. Ricote, R. J. Kee, A. Almansoori, B. P. Gorman and R. P. O'Hayre, *Nano Lett.*, 2016, **16**, 6924–6930.

48 C.-T. Chen, C. E. Danel and S. Kim, *J. Mater. Chem.*, 2011, **21**, 5435–5442.

49 M. F. Yan, R. M. Cannon and H. K. Bowen, *J. Appl. Phys.*, 1983, **54**, 764–778.

50 Z. Wang, L. Ding, S. Yu, H. Xu, X. Hao, Y. Sun and T. He, *ACS Appl. Energy Mater.*, 2022, **5**, 3369–3379.

51 R. Guo, D. Li, R. Guan, D. Kong, Z. Cui, Z. Zhou and T. He, *ACS Sustainable Chem. Eng.*, 2022, **10**, 5352–5362.

52 H. Shimada, T. Yamaguchi, H. Sumi, Y. Yamaguchi, K. Nomura, Y. Mizutani and Y. Fujishiro, *ACS Appl. Energy Mater.*, 2018, **2**, 587–597.

53 Y. Ling, J. Chen, Z. Wang, C. Xia, R. Peng and Y. Lu, *Int. J. Hydrogen Energy*, 2013, **38**, 7430–7437.

54 N. Nasani, D. Ramasamy, S. Mikhalev, A. V. Kovalevsky and D. P. Fagg, *J. Power Sources*, 2015, **278**, 582–589.

55 G. DiGiuseppe, *Ionics*, 2023, 1–8.

56 T. H. Wan, M. Saccoccio, C. Chen and F. Ciucci, *Electrochim. Acta*, 2015, **184**, 483–499.

57 F. Ciucci and C. Chen, *Electrochim. Acta*, 2015, **167**, 439–454.

58 N. Shi, F. Su, D. Huan, Y. Xie, J. Lin, W. Tan, R. Peng, C. Xia, C. Chen and Y. Lu, *J. Mater. Chem. A*, 2017, **5**, 19664–19671.

59 L. Lei, J. M. Keels, Z. Tao, J. Zhang and F. Chen, *Appl. Energy*, 2018, **224**, 280–288.

60 D. Konwar, N. T. Q. Nguyen and H. H. Yoon, *Int. J. Hydrogen Energy*, 2015, **40**, 11651–11658.

61 D. Konwar, B. J. Park, P. Basumatary and H. H. Yoon, *J. Power Sources*, 2017, **353**, 254–259.

62 D. Konwar and H. H. Yoon, *J. Mater. Chem. A*, 2016, **4**, 5102–5106.